Journal of Materials Chemistry A

ROYAL SOCIETY OF CHEMISTRY

PAPER

View Article Online
View Journal | View Issue

Cite this: J. Mater. Chem. A, 2024, 12, 2435

BeN_4 nanoribbon-based 3D porous metallic and ductile monolith for high-performance sodium-ion battery anode†

Wei Sun and Qian Wang *

It is of current interest to design sodium-ion batteries (SIBs) as one of the most promising alternatives to traditional lithium-ion batteries (LIBs). Motivated by the successful synthesis of atomic-thick BeN_4 sheets, going beyond the previously reported three-dimensional (3D) graphene- or silicene-monolith anode materials, we propose a new stable 3D monolith named oBeN_4 by assembling BeN_4 nanoribbons. A combined density functional theory computational study and tight-binding (TB) model analysis revealed that oBeN_4 is mechanically ductile and intrinsically metallic with conducting channels formed by electrons in the p-orbitals of N atoms. Light mass, high porosity, and intrinsic metallicity endow oBeN_4 with superior electrochemical performance when used as an anode material for SIBs, exhibiting a high reversible gravimetric capacity (578.03 mA h g^{-1}) and volumetric capacity (670.51 mA h cm^{-3}), a small volume change (0.5%), low diffusion barriers (0.14–0.68 eV), and a low average open-circuit voltage (0.25 V). These findings demonstrate that the assembly of BeN_4 nanoribbons is a promising strategy for the design of novel SIB anodes with high performance.

Received 30th October 2023
Accepted 15th December 2023

DOI: 10.1039/d3ta06607j

rsc.li/materials-a

1. Introduction

With the constant rising concerns about the high cost and limited terrestrial resources of lithium, SIBs are gradually stepping onto the stage of large-scale energy storage benefiting from the abundant supply of sodium and the similarity in working mechanism to that of LIBs.[1,2] However, the universality of anode materials is far insufficient when it comes to SIBs,[3,4] just like graphite, which serves well for LIBs with a capacity of 372 mA h g^{-1}, possesses a specific capacity as low as 35 mA h g^{-1} when used as the anode for SIBs.[5] Moreover, graphite exhibits a significant volume change when accommodating and transporting Na ions, resulting in poor cycling stability during charging and discharging operations.[6] All these properties are due to the larger ionic radius of Na ions (1.02 Å for Na^+ *vs.* 0.76 Å for Li^+),[7] which seriously hinders the insertion and extraction of Na ions in the anodes.[8] Hence, the design of universal anode materials is urgently required for developing high-performance SIBs.

Since the successful synthesis of 3D graphene monoliths,[9] it has become a new strategy to design 3D porous materials for metal-ion battery anodes using nanoribbons as the building blocks,[10,11] leading to a number of theoretically predicted porous 3D metallic or topological semi-metallic SIB anode materials, including graphene-nanoribbon-assembled bco-C24 (ref. 12) and HZGM-42,[13] silicene-nanoribbon-integrated ISN[14] and 3D-*ortho*-silicene,[15] and biphenylene-nanoribbon-based HexC28.[16] Recently, an atomic-thick BeN_4 sheet[17] has been successfully synthesized in experiments, as predicted by early theoretical work.[18] The polarized bonding between the Be and N atoms could make BeN_4 effective and efficient in storing and transporting Na ions, as is the case with the BeN_4 monolayer for potassium-ion battery anode.[19] It is well known that 3D anode materials are more desirable in practical applications. Therefore, an intriguing question arises: is it possible to design a porous 3D metallic BeN_4 by assembling BeN_4 nanoribbons for high-performance SIB anodes? This motivated us to carry out this study.

2. Computational methods

Our calculations were carried out based on density functional theory (DFT) using the projector augmented wave (PAW) method[20,21] as implemented in the Vienna *ab initio* simulation package (VASP).[22] The generalized gradient approximation (GGA)[23] with the Perdew–Burke–Ernzerhof (PBE) functional was used to treat the electron exchange–correlation interactions for geometry optimization, while the Heyd–Scuseria–Ernzerhof (HSE06) hybrid functional[24,25] was applied for a more accurate electronic band structure. Plane waves with a kinetic energy cutoff of 600 eV were used to expand the wavefunction of valence electrons. High convergence thresholds of 10^{-8} eV and 10^{-6} eV $Å^{-1}$ were set for the total energy and force, respectively. The Brillouin zone is represented by a 3 × 3 × 9 *k*-meshes

School of Materials Science and Engineering, CAPT, Peking University, Beijing 100871, China. E-mail: qianwang2@pku.edu.cn

† Electronic supplementary information (ESI) available. See DOI: https://doi.org/10.1039/d3ta06607j

within the Monkhorst–Pack scheme.[26] To verify the dynamic stability, the finite displacement method[27] implemented in the phonopy code[28] was used with the same convergence criteria. A tight-binding Hamiltonian was constructed to deeply investigate the origin of metallicity by projecting the Bloch states onto the maximally localized Wannier functions based on the WANNIER90 package.[29] Thermal stability was studied by performing *ab initio* molecular dynamics (AIMD)[30] simulations with the Nose–Hoover thermostat.[31] The climbing-image nudged elastic band (CI-NEB) method[32] was used to obtain the diffusion energy barrier profile. In order to study the adsorption and diffusion behavior of Na ions, the effect of van der Waals interactions was considered using the PBE-D2 functional.[33]

3. Results and discussion

3.1 Structure and stability

We used the atomic-thick BeN_4 nanoribbon (Fig. 1a) as the building block and the four-coordinated Be atoms colored in dark green as the cross-linkers (Fig. 1b) to construct the 3D porous monolith, as shown in Fig. 1(c). The formed Be–Be bonding was similar to that in diberyllocene.[34] During the transformation process, the total free energy increased by 0.35 eV per atom, in which the Be–N bond breaking cost was 0.44 eV per atom, while the Be–Be bond formation released −0.09 eV per atom. In other words, the 3D BeN_4 monolith is energetically metastable as compared to the 2D BeN_4 sheet, as is the case with 3D metastable graphene monoliths when compared with 2D graphene sheets. The details can be found in Fig. S1 in the ESI.† Its primitive cell contains 6 Be and 16 N atoms and belongs to the orthorhombic symmetry with the No. 47 space group of *Pmmm* (D2H-1); thus, we named it oBeN_4. In this structure, there are 4 chemically nonequivalent Be and 4 nonequivalent N atoms, occupying the Wyckoff positions of 2j (0.106773, 0, 0.5), 2n (0, 0.175429, 0.5), 1b (0.5, 0, 0), and 1e (0, 0.5, 0), and $4w_1$ (0.232009, 0, 0.182043), $4w_2$ (0.363489, 0, 0.317296), $4u_1$ (0, 0.276065, 0.185234), and $4u_2$ (0, 0.386242, 0.318171). The optimized lattice parameters are $a = 9.53$ Å, $b = 11.44$ Å, $c = 3.66$ Å, and $\alpha = \beta = \gamma = 90°$. Owing to the unique porous configuration displayed in Fig. 1(d), oBeN_4 has a low mass density of 1.16 g cm^{-3}, much lower than that of honeycomb graphene monolith[9] (1.48 g cm^{-3}) and many previously reported low mass density porous structures such as HZGM-42 (1.39 g cm^{-3}),[35] 3D-BPC_2 (1.26 g cm^{-3}),[36] and 3D-Si_2BN (1.41 g cm^{-3}),[37] which have been found to be promising as anode materials for metal ion batteries.

To study the stability of oBeN_4, we first calculated its phonon band spectrum. As shown in Fig. 2(a), there are no imaginary modes in the entire first Brillouin zone, confirming that oBeN_4 is dynamically stable. The thermal stability was then investigated by performing AIMD simulations for 10 ps with the time step of 1 fs within the temperature range from 300 K to 1000 K in 100 K intervals. We find that the geometry exhibits obvious distortion with the chemical bonding between Be atoms broken when the temperature reaches 1000 K. While, the simulated results shown in Fig. 2(b) reveal that the average value of the total potential energy fluctuates slightly around a certain constant during the entire simulation process at 900 K, and the structural skeleton remains almost intact after the simulation, implying that oBeN_4 is thermally stable and can withstand high temperatures up 900 K.

We then adopted the stress–strain method implemented in the AELAS package[38] to calculate the independent elastic constants. According to the symmetry of oBeN_4, there are 9 independent elastic constants,[39] which are calculated from the elastic stiffness matrix to be $C_{11} = 111.33$ GPa, $C_{12} = 0.31$ GPa, $C_{13} = 9.86$ GPa, $C_{22} = 99.57$ GPa, $C_{23} = 7.38$ GPa, $C_{33} = 413.29$ GPa, $C_{44} = 17.10$ GPa, $C_{55} = 20.26$ GPa, and $C_{66} = 0.184$ GPa. While the specific content of Born–Huang criteria for the mechanical stability of the crystals with orthorhombic lattice[40] is $C_{11} > 0$, $C_{11}C_{12} > {C_{12}}^2$, $C_{11}C_{22}C_{33} + 2C_{12}C_{13}C_{23} - C_{11}{C_{23}}^2 - C_{22}{C_{13}}^2 - C_{33}{C_{12}}^2 > 0$, $C_{44} > 0$, $C_{55} > 0$, and $C_{66} > 0$. We find that the calculated constants of oBeN_4 fully satisfy the requirements of the criteria, thereby verifying that oBeN_4 is mechanically stable. Thus, oBeN_4 was determined to be dynamically, thermally, and mechanically stable.

3.2 Mechanical and electronic properties

With the calculated elastic constants of oBeN_4, we first calculated its bulk modulus B, Young's modulus E, and shear modulus G in the framework of the Voigt–Reuss–Hill approximation,[41] where subscripts V, R, and H denote the Vigot bound, Reuss bound, and Hill average, respectively. The results of $B_H = 60.81$ GPa, $E_H = 64.62$ GPa, and $G_H = 24.42$ GPa surpass those of porous ISN with the corresponding values of $B_H = 51.90$ GPa, $E_H = 48.07$ GPa, and $G_H = 20.12$ GPa,[14] implying that this 3D structure can resist external stress in a certain degree. Next, we evaluated the mechanical anisotropy of oBeN_4 using the following equations to obtain the Young's moduli and bulk moduli:[42]

$$E(\boldsymbol{n}) = \frac{1}{{n_1}^4 S_{11} + 2{n_1}^2{n_2}^2 S_{12} + 2{n_1}^2{n_3}^2 S_{13} + {n_2}^4 S_{22} + 2{n_2}^2{n_3}^2 S_{23} + {n_3}^4 S_{33} + {n_2}^2{n_3}^2 S_{44} + {n_1}^2{n_3}^2 S_{55} + {n_1}^2{n_2}^2 S_{66}}.$$

and

$$B(\boldsymbol{n}) = \frac{1}{(S_{11} + S_{12} + S_{13}){n_1}^2 + (S_{12} + S_{22} + S_{23}){n_2}^2 + (S_{13} + S_{23} + S_{33}){n_3}^2}. \quad (1)$$

where, S_{11}, S_{13}, S_{33} and S_{44} represent the elastic compliance constants, and $\boldsymbol{n} = (n_1, n_2, n_3)$ is the unit vector of specific stretching direction. The calculated Young's moduli and bulk

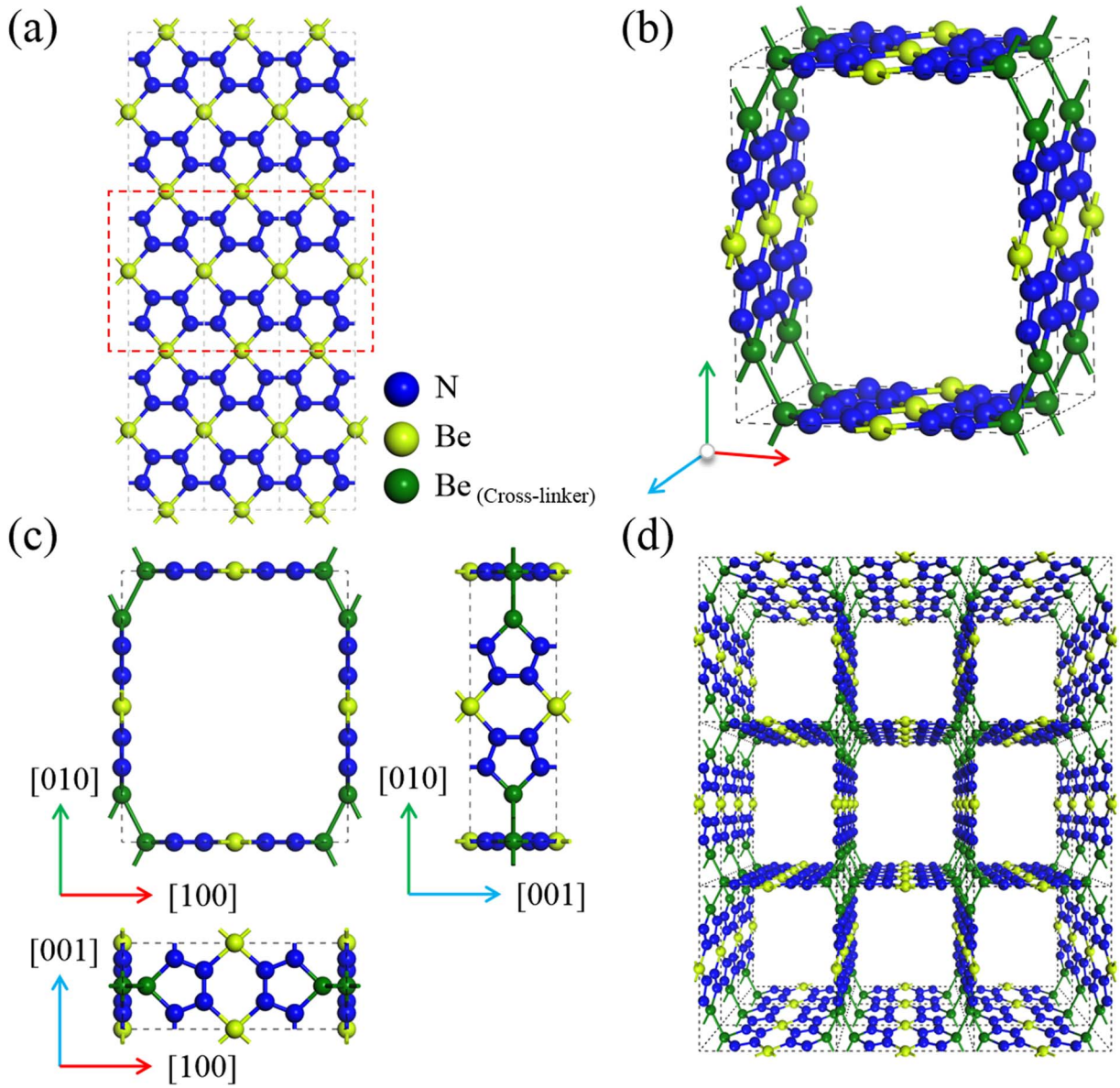

Fig. 1 (a) BeN_4 nanoribbons as the building block. (b) Perspective view of a 1 × 1 × 2 supercell, (c) optimized geometry of the $oBeN_4$ unit cell, and (d) corresponding 3 × 3 × 3 supercell.

moduli along the ***a***, ***b***, and ***c*** directions, namely the [100], [010], and [001], as shown in Fig. 1(c), are $E(\boldsymbol{a}) = 111.09$ GPa, $E(\boldsymbol{b}) = 99.43$ GPa, $E(\boldsymbol{c}) = 411.86$ Gpa, and $B(\boldsymbol{a}) = 113.95$ GPa, $B(\boldsymbol{b}) = 101.36$ GPa, and $B(\boldsymbol{c}) = 491.40$ Gpa, respectively. It is obvious that $oBeN_4$ possesses a stronger resistance to normal deformation in the axial direction than in the other two directions, suggesting that $oBeN_4$ is mechanically anisotropic. We then studied the toughness or brittleness of $oBeN_4$. In general, a material with $\nu > 0.26$ and $G/B < 0.57$ is more likely to exhibit ductile behavior according to Pugh's empirical rule.[43] For $oBeN_4$, the corresponding values were calculated to be $\nu = 0.32$ and $G/B = 0.40$, suggesting that $oBeN_4$ is intrinsically ductile.

To study the electronic properties of $oBeN_4$, we first calculated its electronic band structure at the HSE06 level as it is more accurate than the PBE functional. As plotted in Fig. 3(a), one can see that the partially occupied energy bands cross the Fermi level along the Γ-Z, Z-U, and R-T paths, indicating that $oBeN_4$ is intrinsically metallic. Unlike the reported thickness-dependent semi-metallic feature of the 2D BeN_4 layer,[44] the metallicity of the 3D $oBeN_4$ monolith is enhanced by the rational assembly process. The partial density of states (PDOS), from the HSE06 level, projected on the s- and p-orbitals of Be and N atoms show that the metallicity comes from the p-orbitals of N atoms that contribute the highest density of states near the Fermi level.

To gain a deeper understanding of the origin of the metallicity, we build a TB model in terms of the maximally localized Wannier functions by projecting the Bloch states and using the WANNIER90 code.[29] The Hamiltonian for the p-orbitals of all the nitrogen atoms is defined as:

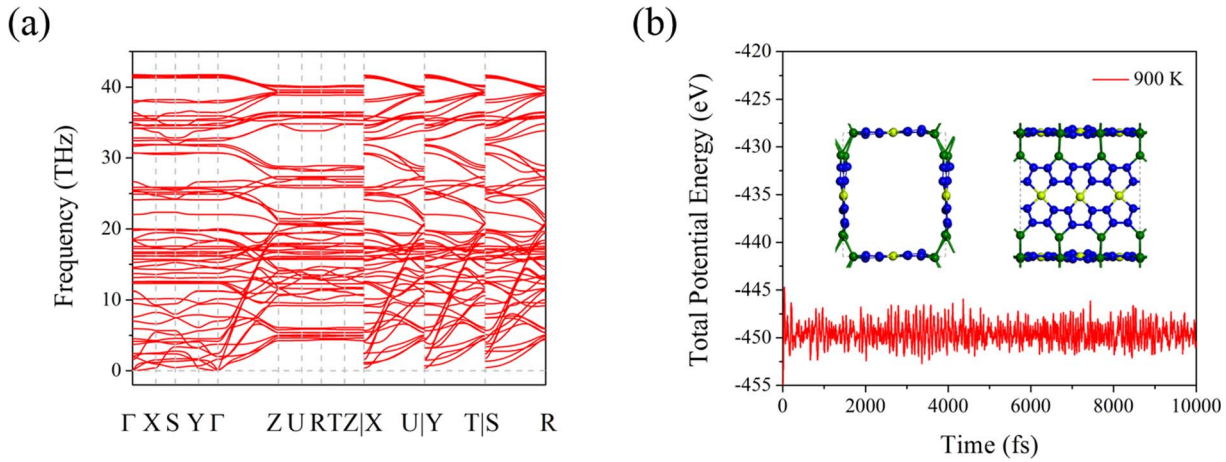

Fig. 2 (a) Phonon band structure, and (b) total potential energy fluctuation of $oBeN_4$ with time during the AIMD simulation at 900 K. Insets show snapshots of the atomic configuration at the end of the simulation.

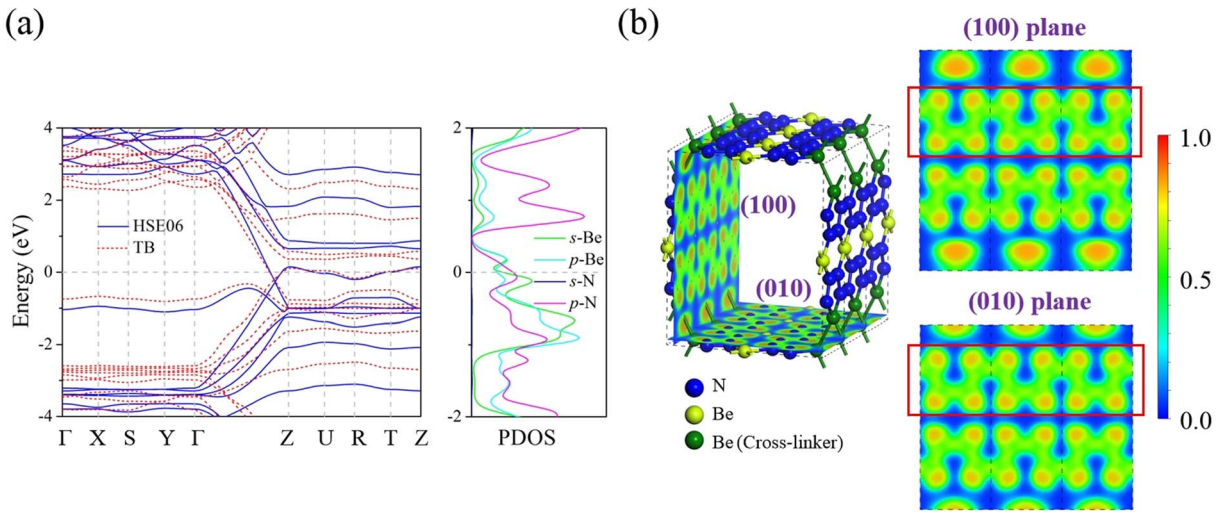

Fig. 3 (a) Electronic band structures from our DFT calculations and the TB model, and PDOS projected on the s and p orbitals of Be and N atoms. (b) Slices of the ELF distribution on the (100) and (010) lattice planes of $oBeN_4$.

$$H = \varepsilon_0 \sum_i c_i^\dagger c_i + \sum_{ij} \left(t_{ij} c_i^\dagger c_j + H.c. \right). \quad (2)$$

where, $c_i^\dagger$, c_i, ε_0, and t_{ij} correspond to the electronic creation and annihilation operators of the p-orbital at site i, the on-site energy, and the hopping integral describing the jumping process of electrons from the i site to j site, respectively. By projecting the p-orbitals of all N atoms in the unit cell, the electronic band structure calculated from the TB model is presented in Fig. 3(a) with a red dashed line for comparison. One can see that the band structure characteristics near the Fermi level are well consistent with those obtained from our DFT calculation, further confirming that the origin of metallicity comes from the electrons in the p-orbitals of all the N atoms in $oBeN_4$.

We further calculated the electron localization function (ELF)[45] for BeN_4 to obtain a specific electronic distribution, and to examine if any electron conducting channel exists in this structure. ELF has been widely used to measure electron localization by describing the electron distribution in materials with its value ranging from 0.0 to 1.0. The value of 1.0 corresponds to the perfect localization, 0.5 to the electron-gas-like behavior, and 0.0 corresponds to the state with extremely low charge density.[46] The electron density distributions in the (100) and (010) planes, shown in Fig. 3(b), indicate that the conducting channels are along the N-chains, where the p-orbitals of the N atoms contribute to the intrinsic metallicity of $oBeN_4$.

3.3 Performance as an anode material for SIBs

Considering its structural porosity, mechanical ductility, and intrinsic metallicity, $oBeN_4$ can be expected to be promising for high reversible capacity, improved cycling stability, and enhanced rate performance when used as an anode for SIBs. Hence, we calculated the related parameters, including the theoretical reversible capacity, diffusion energy barrier, volume expansion, and average open-circuit voltage.

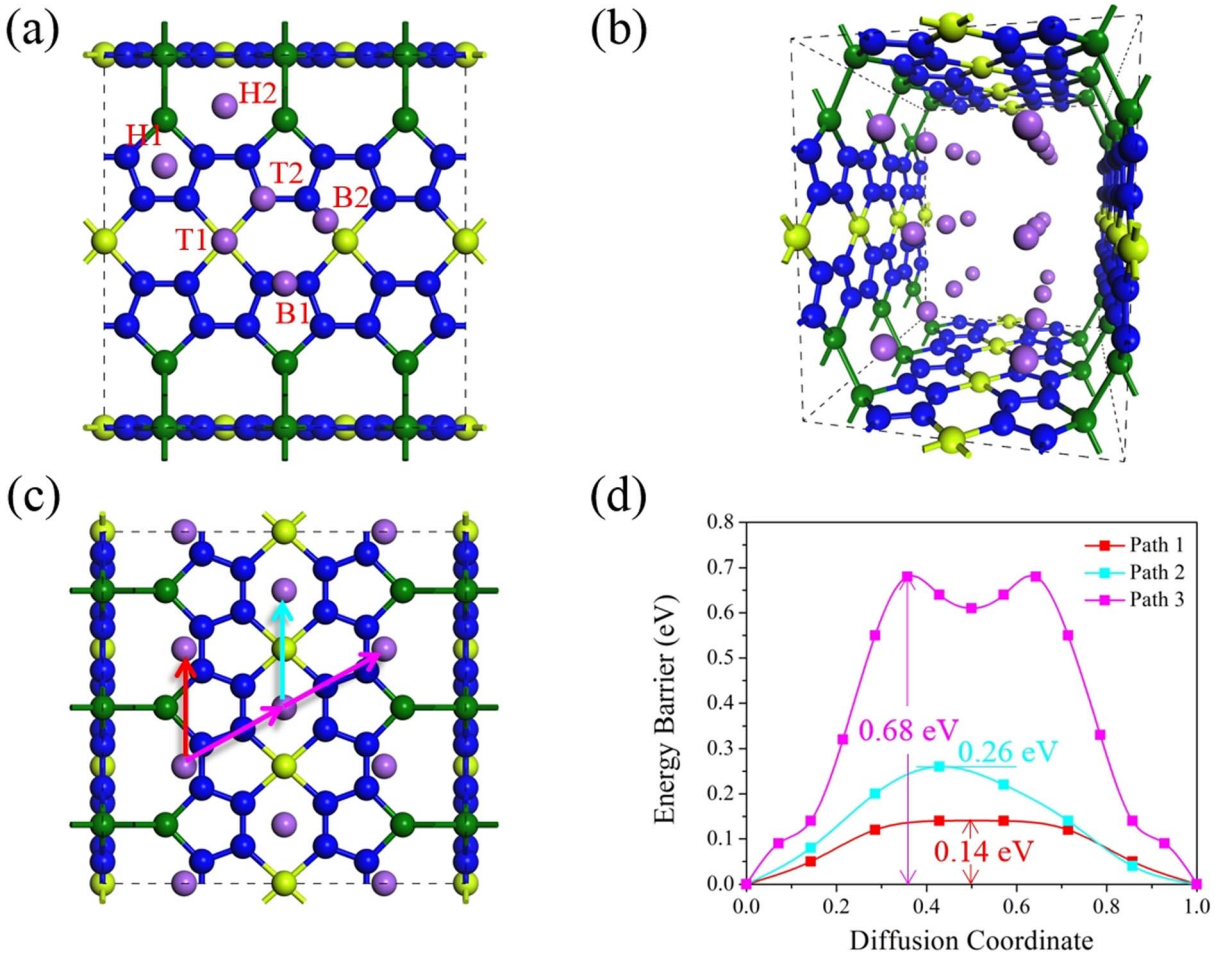

Fig. 4 (a) All possible adsorption sites for a single Na atom in $oBeN_4$. (b) Perspective and (c) orthographic view of the fully sodiated $oBeN_4$ configuration with different diffusion paths, and (d) the corresponding energy barrier.

To find suitable absorption sites for a single Na atom in the $oBeN_4$ substrate, we first studied the binding strength of Na atoms at different potential sites. A $1 \times 1 \times 3$ supercell was used for the calculations to prevent the interaction between the Na atoms. All nonequivalent possible sites can be divided into three types: the bridge site (B) over the atomic bonds, the hollow site (H) above the center of the atomic rings, and the top site (T) on the top of atoms, as shown in Fig. 4(a). To measure the adsorption strength of every possible site, we calculated the binding energy E_b using the following equation.

$$E_b = (E_{Na_n-oBeN_4} - E_{oBeN_4} - n\mu_{Na})/n. \quad (3)$$

where, $E_{Na_n-oBeN_4}$, E_{oBeN_4}, μ_{Na} and n are the total energy of the system with and without the adsorbed Na atoms, the energy of one Na atom in its bulk form, and the number of the Na atoms in the supercell, respectively. After full optimization, Na atoms on the different candidate sites move to the H2 site or its equivalents. The corresponding binding energy is calculated to be −0.25 eV, indicating that the H2 site is the energetically most favorable adsorption site for a single Na atom. Based on the analysis of the Bader charge transfer,[47] we find that Na ion transfers 0.86 electrons to the substrate upon adsorption, providing the required Na^+ ions for battery operation.

Next, we calculated the maximal theoretical capacity of $oBeN_4$ by gradually increasing the concentration of the absorbed Na ions on the energetically most favorable adsorption site and its equivalents until an energetically unfavorable state is reached. In this process, we considered not only all the equivalent stable adsorption sites but also the symmetry and distance between the Na ions to avoid clustering. The final configuration is presented in Fig. 4(b) and (c) from the perspective and orthographic view, respectively. The resulting chemical stoichiometric ratio is such that one $oBeN_4$ unit cell can maximally store 6 Na ions. Hence, we can calculate the corresponding maximal theoretical gravimetric capacity (C_M) and volumetric capacity (C_V) based on the following formulae:

$$C_M = \frac{n_m F}{M}, C_V = \frac{n_m F}{V}. \quad (4)$$

where n_m represents the maximum adsorption number of Na ions, F is the Faraday constant with a value of 26.8 A h mol^{-1}, and M and V are the mass and volume of the $oBeN_4$ substrate, respectively. The values of gravimetric capacity and volumetric

capacity were calculated to be 578.03 mA h g^{-1} and 670.51 mA h cm^{-3}, respectively, which are much larger than those experimentally observed for graphite (35 mA h g^{-1})[5,8] and hard carbon (230 mA h g^{-1}).[48] Such theoretical capacity is not only higher than that of many theoretically designed 3D porous metallic/semi-metallic carbon allotropes such as HZGM-42 (318.5 mA h g^{-1}),[13] penta-oC36 (496.9 mA h g^{-1}),[49] and oC46 (303 mA h g^{-1}),[50] but also surpasses the capacity of some other SIB anodes composed of light elements other than carbon, including ISN (159.5 mA h g^{-1}),[14] 3D-BPC_2 (407.29 mA h g^{-1}),[36] and 3D-Si_2BN (341.61 mA h g^{-1}).[37] Such obvious advantages in theoretical capacity are attributed to its characteristics of well-sized pores and light constituent elements, suggesting that $oBeN_4$ can store large amounts of Na ions when serving as the anode for SIBs.

To study the transport behavior of Na ions in the $oBeN_4$ anode, we used the CI-NEB method[32] for the calculation of the energy profile to determine the diffusion energy barrier. Based on the symmetry of the geometric configuration and adsorption sites, three nonequivalent migration paths were selected, as shown in Fig. 4(c), where two are along the conducting channel and one crosses between them. The calculated results are plotted in the diffusion profiles in Fig. 4(d), which shows that the energy barrier for Na ions ranges from 0.14 to 0.26 eV along the axial paths, and path 1 is the energetically most favorable path. The energy barrier is 0.68 eV when Na ions diffuse across these two diffusion paths, implying that it is also possible for Na ions to switch diffusion channels during the transporting process. In addition, we also studied the situation with high Na-ion concentration by investigating the diffusion behavior of a single vacancy. The results are presented in Fig. S2.† The minimum diffusion energy barrier is lower than that of graphite (0.40 eV),[8] HexC28 (0.22 eV),[16] C-honeycomb (0.17 eV),[51] and experimentally synthesized Si_{24} (0.68 eV).[52,53] This implies that the stored Na ions can migrate easily due to the intrinsic metallicity and regularly distributed conducting channels in the $oBeN_4$ structure, leading to a good rate of performance when used as anode materials in SIBs.

To further study the performance of $oBeN_4$ when used as the anode for SIBs, we carried out the half-cell reaction *versus* Na/Na^+ based on the following equation for the charging/discharging process:

$$(x_2 - x_1)Na^+ + (x_2 - x_1)e^- + Na_{x_1} - oBeN_4 \leftrightarrow Na_{x_2} - oBeN_4. \quad (5)$$

where x_1 and x_2 refer to different Na concentrations in the $oBeN_4$ system. Although we previously obtained the maximal theoretical capacity of the $oBeN_4$ anode for SIBs as 578.03 mA h g^{-1}, specific adsorption states under different intermediate concentrations were not determined. Using the Ewald energy method implemented in pymatgen software,[54,55] we generate a series of symmetrically nonequivalent configurations with Na-ion concentration of $x = 0.167$, $x = 0.333$, $x = 0.500$, $x = 0.667$, and $x = 0.833$. To compare the energies of the fully optimized possible structures, the energetically most stable configuration under a given concentration was used as the ground state structure. Based on these selected stable intermediate states and eqn (3), we calculate the adsorption energy under different concentrations and the corresponding variation curve is given in Fig. 5(a), which shows that the binding strength gradually weakens as the concentration increases due to the strengthened Coulomb repulsion among Na ions.

To check the thermodynamic stability of the most favorable Na-intercalated configurations, we plotted the equilibrium convex hull based on their corresponding formation energy E_f using the following equation:

$$E_f = E_{Na_x-oBeN_4} - (1 - x)E_{oBeN_4} - xE_{Na-oBeN_4}. \quad (6)$$

where, $E_{Na_x-oBeN_4}$, E_{oBeN_4}, and $E_{Na-oBeN_4}$ are the total energies of the energetically most favorable Na-intercalated system with concentrations of x, 0, and 1, respectively. As shown in Fig. 5(b), one can see that these selected configurations with the Na-ion concentrations of 0.167, 0.667, and 0.833 are thermodynamically stable. Based on these thermodynamic ground-state configurations, we further evaluate the average voltage V using the following formula:

$$V \approx \frac{E_{Na_{x_1}-oBeN_4} - E_{Na_{x_2}-oBeN_4} + (x_2 - x_1)\mu_{Na}}{x_2 - x_1}. \quad (7)$$

where, $E_{Na_{x_1}-oBeN_4}$ and $E_{Na_{x_2}-oBeN_4}$ are the total energies of the Na ion intercalated system with the concentration of x_1 and x_2, respectively. The calculated voltage profile in the half-cell model is displayed in Fig. 5(c), in which the voltage is always positive during the entire operation, indicating that the maximal

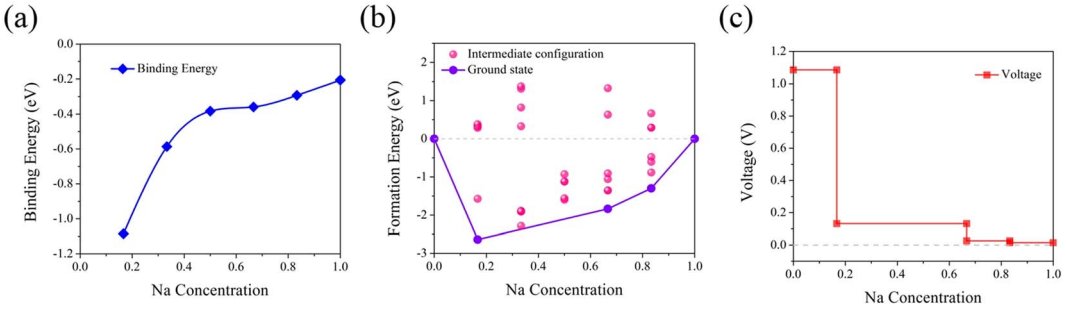

Fig. 5 (a) Adsorption energy curve, (b) ground-state hull of intermediate Na-intercalated configurations, and (c) calculated voltage profile in the half-cell model for $oBeN_4$.

Table 1 Comparison of the key properties of the $oBeN_4$ anode with some previously reported anode materials for SIBs

Structure	Reversible capacity (mA h g^{-1})	Volume change (%)	Diffusion barrier (eV)	Average open-circuit voltage (V)	Electronic property
$oBeN_4$	578.03	0.5	0.14	0.25	Metallic
HZGM-42 (ref. 13)	318.5	1.85	0.08	0.43	Semi-metallic
tC_{24} (ref. 56)	232.65	0.94	0.053	0.54	Semi-metallic
ISN[14]	159.5	2.80	0.005	1.35	Semi-metallic
Si_{24} (ref. 52 and 53)	159	2.30	0.68	0.30	Metallic
SiC_4–I[57]	176.3	0.57	0.410	0.55	Metallic
3D-BPC_2 (ref. 36)	407.29	1.15	0.05	0.50	Metallic
3D-Si_2BN[37]	341.61	2.7	0.19	0.15	Semiconducting
Graphite with co-intercalation reactions[8,58]	109	80	0.40	0.66	Metallic

reversible gravimetric capacity is 578.03 mA h g^{-1} and reversible volumetric capacity is 670.51 mA h cm^{-3} for $oBeN_4$. We further calculated the average open-circuit voltage by evaluating the numerical average of the voltage curve within the entire concentration range and found the corresponding value of 0.25 V, which is lower than the value of HZGM-42 (0.43 V),[13] penta-oC36 (0.39 V),[49] ISN (1.35 V),[14] and 3D-BPC_2 (0.50 V).[36] Such low voltage in the half-cell model can increase the fuel cell's operating voltage when the $oBeN_4$ anode is connected to the cathode, further enhancing the energy density of the SIBs.

To check the cycling stability, we calculated the overall volume change during the charging/discharging process using the following formula:

$$\Delta\Omega = \frac{\Omega_{Na} - \Omega_0}{\Omega_0} \times 100\%. \quad (8)$$

where, Ω_{Na} and Ω_0 are the volumes of the Na-intercalated and empty $oBeN_4$ systems, respectively. The charging/discharging process represents the sodiation/desodiation behavior of Na ions, so the empty and full Na-intercalated $oBeN_4$ systems are two boundary states. Hence, we calculated the respective volume of each one and compared them to obtain the total volume change to be 0.5%, which was much smaller than that of HZGM-42 (1.85%),[13] ISN (2.80%),[14] 3D-BPC_2 (1.15%),[36] and 3D-Si_2BN (2.7%).[37] Such excellent cycling stability is attributed to its intrinsic ductility, proving that $oBeN_4$ can possess long-term cycle life when used as the anode for SIBs.

For a better understanding of the performance of $oBeN_4$, comparisons were made with some experimentally synthesized and theoretically designed SIBs anode materials, including silicon carbides, graphene-nanoribbon-based HZGM-42, silicene-nanoribbon-based ISN, BPC_2-nanoribbon-based 3D-BPC_2, and Si_2BN-nanoribbon-based 3D-Si_2BN, as shown in Table 1. It is obvious that the BeN_4-nanoribbon-based $oBeN_4$ is a promising anode material of SIBs with a high theoretical reversible capacity, good rate performance, and a long-term cycle life.

4. Conclusions

In brief, in contrast to various previously designed nanoribbon-based anode materials, for the first time, we propose a new 3D porous monolith named $oBeN_4$ based on experimentally synthesized 2D BeN_4 nanoribbons and the newly developed strategy of Be–Be bond formation. Using DFT calculations combined with the tight-binding model and phase diagram analysis, we not only verified the dynamic, thermal, and mechanical stability of $oBeN_4$ but also proved its mechanical ductility and intrinsic metallicity originating from the electrons in the p-orbitals of N atoms. We further demonstrated that as a promising anode for SIBs, $oBeN_4$ possesses a high reversible gravimetric capacity of 578.03 mA h g^{-1} and volumetric capacity of 670.51 mA h cm^{-3}, a small volume change of 0.5%, a low diffusion barrier of 0.14 eV, and a low average open-circuit voltage of 0.25 V, surpassing the performance of the other reported systems to some extent. We expect that our study will stimulate further efforts in synthesizing such 3D nanoribbon-based anodes for SIBs with high performance.

Conflicts of interest

There are no conflicts of interest to declare.

Acknowledgements

This work was partially supported by grants from the National Natural Science Foundation of China (Grants No. NSFC-11974028 and NSFC-12274007), and is also supported by the high-performance computing platform of Peking University, China.

References

1 J.-Y. Hwang, S.-T. Myung and Y.-K. Sun, Sodium-ion batteries: present and future, *Chem. Soc. Rev.*, 2017, **46**, 3529–3614.
2 S. Alvin, H. S. Cahyadi, J. Hwang, W. Chang, S. K. Kwak and J. Kim, Revealing the intercalation mechanisms of lithium, sodium, and potassium in hard carbon, *Adv. Energy Mater.*, 2020, **10**, 2000283.
3 V. L. Chevrier and G. Ceder, Challenges for Na-ion negative electrodes, *J. Electrochem. Soc.*, 2011, **158**, A1011.
4 J. Xu, M. Wang, N. P. Wickramaratne, M. Jaroniec, S. Dou and L. Dai, High-performance sodium ion batteries based

on a 3D anode from nitrogen-doped graphene foams, *Adv. Mater.*, 2015, **27**, 2042–2048.

5 C. Yang, X. Sun, X. Zhang, J. Li, J. Ma, Y. Li, L. Xu, S. Liu, J. Yang, S. Fang, Q. Li, X. Yang, F. Pan, J. Lu and D. Yu, Is graphite nanomesh a promising anode for the Na/K-Ions batteries?, *Carbon*, 2021, **176**, 242–252.

6 Y. Wen, K. He, Y. Zhu, F. Han, Y. Xu, I. Matsuda, Y. Ishii, J. Cumings and C. Wang, Expanded graphite as superior anode for sodium-ion batteries, *Nat. Commun.*, 2014, **5**, 4033.

7 W. Luo, F. Shen, C. Bommier, H. Zhu, X. Ji and L. Hu, Na-ion battery anodes: materials and electrochemistry, *Acc. Chem. Res.*, 2016, **49**, 231–240.

8 H. Hou, X. Qiu, W. Wei, Y. Zhang and X. Ji, Carbon anode materials for advanced sodium-ion batteries, *Adv. Energy Mater.*, 2017, **7**, 1602898.

9 N. V. Krainyukova and E. N. Zubarev, Carbon honeycomb high capacity storage for gaseous and liquid species, *Phys. Rev. Lett.*, 2016, **116**, 055501.

10 J. Li, J. Xu, Z. Xie, X. Gao, J. Zhou, Y. Xiong, C. Chen, J. Zhang and Z. Liu, Diatomite-templated synthesis of freestanding 3D graphdiyne for energy storage and catalysis application, *Adv. Mater.*, 2018, **30**, 1800548.

11 M. M. Obeid and Q. Sun, Assembling biphenylene into 3D porous metallic carbon allotrope for promising anode of lithium-ion batteries, *Carbon*, 2022, **188**, 95–103.

12 S. Wang, B. Yang, E. Ruckenstein and H. Chen, Bco-C24: a new 3D Dirac nodal line semi-metallic carbon honeycomb for high performance metal-ion battery anodes, *Carbon*, 2020, **159**, 542–548.

13 Y. Shen, Q. Wang, Y. Kawazoe and P. Jena, Potential of porous nodal-line semi-metallic carbon for sodium-ion battery anode, *J. Power Sources*, 2020, **478**, 228746.

14 Y. Qie, J. Liu, X. Li, S. Wang, Q. Sun and P. Jena, Interpenetrating silicene networks: a topological nodal-line semimetal with potential as an anode material for sodium ion batteries, *Phys. Rev. Mater.*, 2018, **2**, 084201.

15 I. Muhammad, S. Ahmed, H. Cao, A. Mahmood and Y. Wang, Three-dimensional silicene-based materials: a universal anode for monovalent and divalent ion batteries, *J. Phys. Chem. C*, 2023, **127**, 1198–1208.

16 M. M. Obeid, D. Ni, P. Du and Q. Sun, Design of three-dimensional metallic biphenylene networks for Na-ion battery anodes with a record high capacity, *ACS Appl. Mater. Interfaces*, 2022, **14**, 32043–32055.

17 M. Bykov, T. Fedotenko, S. Chariton, D. Laniel, K. Glazyrin, M. Hanfland, J. S. Smith, V. B. Prakapenka, M. F. Mahmood, A. F. Goncharov, A. V. Ponomareva, F. Tasnádi, A. I. Abrikosov, T. B. Masood, I. Hotz, A. N. Rudenko, M. I. Katsnelson, N. Dubrovinskaia, L. Dubrovinsky and I. A. Abrikosov, High-pressure synthesis of Dirac materials: layered van der Waals bonded BeN_4 polymorph, *Phys. Rev. Lett.*, 2021, **126**, 175501.

18 S. Zhang, Z. Zhao, L. Liu and G. Yang, Pressure-induced stable BeN_4 as a high-energy density material, *J. Power Sources*, 2017, **365**, 155–161.

19 Z. Cheng, X. Zhang, H. Zhang, H. Liu, X. Yu, X. Dai, G. Liu and G. Chen, BeN_4 monolayer as an excellent Dirac anode material for potassium-ion batteries, *J. Alloys Compd.*, 2023, **936**, 168351.

20 P. E. Blöchl, Projector augmented-wave method, *Phys. Rev. B: Condens. Matter Mater. Phys.*, 1994, **50**, 17953–17979.

21 G. Kresse and D. Joubert, From ultrasoft pseudopotentials to the projector augmented-wave method, *Phys. Rev. B: Condens. Matter Mater. Phys.*, 1999, **59**, 1758–1775.

22 G. Kresse and J. Furthmüller, Efficient iterative schemes for *ab initio* total-energy calculations using a plane-wave basis set, *Phys. Rev. B: Condens. Matter Mater. Phys.*, 1996, **54**, 11169–11186.

23 J. P. Perdew, K. Burke and M. Ernzerhof, Generalized gradient approximation made simple, *Phys. Rev. Lett.*, 1996, **77**, 3865–3868.

24 J. Heyd, G. E. Scuseria and M. Ernzerhof, Hybrid functionals based on a screened Coulomb potential, *J. Chem. Phys.*, 2003, **118**, 8207–8215.

25 J. Heyd, G. E. Scuseria and M. Ernzerhof, Erratum: hybrid functionals based on a screened Coulomb potential, *J. Chem. Phys.*, 2003, **118**, 8207; *J. Chem. Phys.*, 2006, **124**, 219906.

26 H. J. Monkhorst and J. D. Pack, Special points for Brillouin-zone integrations, *Phys. Rev. B: Solid State*, 1976, **13**, 5188–5192.

27 K. Parlinski, Z. Q. Li and Y. Kawazoe, First-principles determination of the soft mode in cubic ZrO_2, *Phys. Rev. Lett.*, 1997, **78**, 4063–4066.

28 A. Togo and I. Tanaka, First principles phonon calculations in materials science, *Scr. Mater.*, 2015, **108**, 1–5.

29 A. A. Mostofi, J. R. Yates, Y.-S. Lee, I. Souza, D. Vanderbilt and N. Marzari, wannier90: a tool for obtaining maximally-localised Wannier functions, *Comput. Phys. Commun.*, 2008, **178**, 685–699.

30 D. Bucher, L. C. T. Pierce, J. A. McCammon and P. R. L. Markwick, On the use of accelerated molecular dynamics to enhance configurational sampling in *ab initio* simulations, *J. Chem. Theory Comput.*, 2011, **7**, 890–897.

31 D. Evans and B. Holian, The Nose–Hoover thermostat, *J. Chem. Phys.*, 1985, **83**, 4069–4074.

32 G. Mills and H. Jónsson, Quantum and thermal effects in H_2 dissociative adsorption: evaluation of free energy barriers in multidimensional quantum systems, *Phys. Rev. Lett.*, 1994, **72**, 1124–1127.

33 S. Grimme, Semiempirical GGA-type density functional constructed with a long-range dispersion correction, *J. Comput. Chem.*, 2006, **27**, 1787–1799.

34 J. T. Boronski, A. E. Crumpton, L. L. Wales and S. Aldridge, Diberyllocene, a stable compound of Be(I) with a Be-Be bond, *Science*, 2023, **380**, 1147–1149.

35 J. Liu, X. Li, Q. Wang, Y. Kawazoe and P. Jena, A new 3D Dirac nodal-line semi-metallic graphene monolith for lithium ion battery anode materials, *J. Mater. Chem. A*, 2018, **6**, 13816–13824.

36 U. Younis, I. Muhammad, F. Qayyum, Y. Kawazoe and Q. Sun, A stable metallic 3D porous BPC_2 as a universal anode material for Li, Na, and K ion batteries with high performance, *J. Mater. Chem. A*, 2020, **8**, 25824–25830.

37 U. Younis, I. Muhammad, W. Wu, S. Ahmed, Q. Sun and P. Jena, Assembling Si_2BN nanoribbons into a 3D porous structure as a universal anode material for both Li- and Na-ion batteries with high performance, *Nanoscale*, 2020, **12**, 19367–19374.
38 S. H. Zhang and R. F. Zhang, AELAS: automatic ELAStic property derivations *via* high-throughput first-principles computation, *Comput. Phys. Commun.*, 2017, **220**, 403–416.
39 Z. Wu, E. Zhao, H. Xiang, X. Hao, X. Liu and J. Meng, Crystal structures and elastic properties of superhard IrN_2 and IrN_3 from first principles, *Phys. Rev. B: Condens. Matter Mater. Phys.*, 2007, **76**, 054115.
40 F. Mouhat and F.-X. Coudert, Necessary and sufficient elastic stability conditions in various crystal systems, *Phys. Rev. B: Condens. Matter Mater. Phys.*, 2014, **90**, 224104.
41 R. Hill, The elastic behaviour of a crystalline aggregate, *Proc. Phys. Soc., London, Sect. A*, 1952, **65**, 349–354.
42 J. Yang and J. Zheng, Electronic properties, anisotropic elasticity, theoretical strengths, and lattice vibrational mode of orthorhombic YSi, *Solid State Commun.*, 2020, **321**, 114029.
43 S. F. Pugh, XCII. Relations between the elastic moduli and the plastic properties of polycrystalline pure metals, *London, Edinburgh Dublin Philos. Mag. J. Sci.*, 1954, **45**, 823–843.
44 A. Bafekry, C. Stampfl, M. Faraji, M. Yagmurcukardes, M. M. Fadlallah, H. R. Jappor, M. Ghergherehchi and S. A. H. Feghhi, A Dirac-semimetal two-dimensional BeN_4: thickness-dependent electronic and optical properties, *Appl. Phys. Lett.*, 2021, **118**, 203103.
45 A. D. Becke and K. E. Edgecombe, A simple measure of electron localization in atomic and molecular systems, *J. Chem. Phys.*, 1990, **92**, 5397–5403.
46 A. Savin, R. Nesper, S. Wengert and T. F. Fässler, ELF: the electron localization function, *Angew Chem. Int. Ed. Engl.*, 1997, **36**, 1808–1832.
47 W. Tang, E. Sanville and G. Henkelman, A grid-based Bader analysis algorithm without lattice bias, *J. Phys.: Condens. Matter*, 2009, **21**, 084204.
48 S. Komaba, W. Murata, T. Ishikawa, N. Yabuuchi, T. Ozeki, T. Nakayama, A. Ogata, K. Gotoh and K. Fujiwara, Electrochemical Na insertion and solid electrolyte interphase for hard-carbon electrodes and application to Na-ion batteries, *Adv. Funct. Mater.*, 2011, **21**, 3859–3867.
49 S. Li, Y. Shen, D. Ni and Q. Wang, A new 3D metallic carbon allotrope composed of penta-graphene nanoribbons as a high-performance anode material for sodium-ion batteries, *J. Mater. Chem. A*, 2021, **9**, 23214–23222.
50 D. Ni, Y. Shen, W. Sun and Q. Wang, Design of 3D topological nodal-net porous carbon for sodium-ion battery anodes, *J. Mater. Chem. A*, 2022, **10**, 7754–7763.
51 L. Shi, A. Xu and T. Zhao, Three-dimensional carbon-honeycomb as nanoporous lithium and sodium deposition scaffold, *J. Phys. Chem. C*, 2018, **122**, 21262–21268.
52 D. Y. Kim, S. Stefanoski, O. O. Kurakevych and T. A. Strobel, Synthesis of an open-framework allotrope of silicon, *Nat. Mater.*, 2014, **14**, 169–173.
53 U. Arrieta, N. A. Katcho, O. Arcelus and J. Carrasco, First-principles study of sodium intercalation in crystalline Na_xSi_{24} ($0 \leq x \leq 4$) as anode material for Na-ion batteries, *Sci. Rep.*, 2017, **7**, 5350.
54 S. P. Ong, W. D. Richards, A. Jain, G. Hautier, M. Kocher, S. Cholia, D. Gunter, V. L. Chevrier, K. A. Persson and G. Ceder, Python Materials Genomics (pymatgen): a robust, open-source python library for materials analysis, *Comput. Mater. Sci.*, 2013, **68**, 314–319.
55 S. Wang, Q. Bai, A. M. Nolan, Y. Liu, S. Gong, Q. Sun and Y. Mo, Lithium chlorides and bromides as promising solid-state chemistries for fast ion conductors with good electrochemical stability, *Angew. Chem., Int. Ed.*, 2019, **58**, 8039–8043.
56 Y. Qie, J. Liu, S. Wang, Q. Sun and P. Jena, Tetragonal C_{24}: a topological nodal-surface semimetal with potential as an anode material for sodium ion batteries, *J. Mater. Chem. A*, 2019, **7**, 5733–5739.
57 Y. Qie, S. Wang and Q. Sun, Three dimensional metallic porous SiC_4 allotropes: stability and battery applications, *Nano Energy*, 2019, **63**, 103862.
58 Z. Xu, G. Yoon, K. Park, H. Park, O. Tamwattana, S. J. Kim, W. M. Seong and K. Kang, Tailoring sodium intercalation in graphite for high energy and power sodium ion batteries, *Nat. Commun.*, 2019, **10**, 2598.